Interfacial creation of positively charged sites in LaPO$_4$/Fe$_3$(PO$_4$)$_2$ heterojunctions for high-current-density oxygen evolution

Sitong Liu,[a,b]   Yudi Zhang, [b,c]   Wen Sun,[b,c] Junqiang Wang[b,c], Dengsong Zhang,[a]*
Juntao Huo[b,c]*, Guowei Li[b,c]*

a. State Key Laboratory of Advanced Special Steel, School of Materials Science and Engineering, International Joint Laboratory of Catalytic Chemistry, College of Sciences, Shanghai University, Shanghai 200444, China
b. CAS Key Laboratory of Magnetic Materials and Devices, Ningbo Institute of Materials Technology and Engineering, Chinese Academy of Sciences, Ningbo 315201, China
c. Center of Materials Science and Optoelectronics Engineering, University of Chinese Academy of Sciences, Beijing 100049, China.

1 Experimental Section

1.1. Materials and reagents

Lanthanum nitrate hexahydrate (La(NO$_3$)$_3$·6H$_2$O), ferric nitrate nonahydrate (Fe(NO$_3$)$_3$·9H$_2$O), melamine, and diaminium hydrogen phosphate were purchased from Aladdin's Reagent Co. All chemicals were of analytical grade without any further purification.

1.2 Preparation of MPO$_4$ (M=La,Fe)

1 mmol of 1 M(NO$_3$)$_X$·YH$_2$O, 1 mmol of melamine，and 8 mmol of diammonium phosphate were dissolved in deionized water and sonicated to ensure complete dissolution and uniform mixing. The resulting solution was then poured onto nickel foam in a crucible and dried at 75°C. The nickel foam was then transferred to a tubular furnace, where the temperature was gradually increased to 500°C over 40 minutes under a hydrogen and argon atmosphere. The temperature was held at 500°C for 2 hours under a flow of hydrogen gas. After cooling to room temperature, the nickel mold and powder were washed multiple times with deionized water and ethanol.

1.3 Preparation of LaPO$_4$/Fe$_3$(PO$_4$)$_2$

Similarly, 1 mmol of La(NO$_3$)$_3$·6H$_2$O, 2 mmol of Fe(NO$_3$)$_3$·9H$_2$O, 1 mmol of melamine, and 8 mmol of diammonium phosphate were dissolved in deionized water, followed by sonication to ensure complete dissolution and homogeneous mixing. The resulting solution was then transferred onto nickel foam in a crucible and dried at 75°C. After drying, the nickel foam was then transferred to a tubular furnace. Under a mixed atmosphere of hydrogen (H$_2$) and argon (Ar), the temperature was ramped up to 500°C over 40 minutes, and held at this temperature for 2 hours with a continuous flow of hydrogen gas. After cooling to room temperature, the nickel foam and the powder were washed multiple times with deionized water and ethanol.

1.4 Characterization

The phase structure of the catalyst was characterized using X-ray diffraction (XRD, Bruker, D8 ADVANCE). Scanning electron microscopy (SEM) images and corresponding energy-dispersive spectroscopy (EDS) elemental analyses were

recorded using a FEI Quanta FEG 250 electron microscope equipped with an acceleration voltage of 15 kV. Raman spectroscopy (Renishaw inVia Reflex) was used to characterise the structure and properties of the functional groups of the material. The ultraviolet-visible (UV–vis) spectrophotometer (Lambda 950) with barium sulfate as the reference was employed for collecting the UV–vis diffuse-reflectance. The surface of the pristine catalyst and their elemental distributions were examined using transmission electron microscopy (TEM, Talos F200x) and double-corrected transmission electron microscopy (AC-TEM, Spectra 300), along with energy-dispersive X-ray spectroscopy (EDS) analysis. The surface chemical state and binding energies of the samples were obtained via X-ray photoelectron spectroscopy (XPS, Kratos, Axis Ultra DLD), with peak calibration performed against adventitious carbon (C 1s at 284.8 eV). The XPS spectra of the samples were curve-fitted and deconvoluted using the Casa XPS software.

2.5 Electrochemical characterization

All electrochemical measurements were performed at room temperature on an Autolab PGSTAT302N electrochemical workstation with impedance module. A typical three-electrode configuration was used, with a carbon rod as counter electrode and an Ag/AgCl electrode (3 M KCl) as reference electrode. The working electrode was nickel foam equipped with catalyst. Linear scanning voltammetry (LSV) experiments were performed in 1 M KOH or electrolyte at a scan rate of 5 mV s^{-1}, compensating for 100% of the iR based on the solution resistance in the impedance spectra. we calculated the current density based on the actual geometric surface area of the electrode. All potentials reported in this study were converted to reversible hydrogen electrodes according to the following equation:

$$E \text{ (versus RHE)} = E \text{ (versus Ag/AgCl)} + (0.2046 + 0.059 \text{ pH}) \text{ V.} \qquad (1)$$

The potentials reported in this study were converted to reversible hydrogen electrodes according to the following equation. The electrochemical impedance spectroscopy (EIS) was performed in the frequency range of 100 kHz-0.1 Hz with an amplitude of 0.01 mV.

Stability tests were performed with a time-varying potentiostat at a current density

of 500 mA cm^{-2} and without iR compensation. Oxygen was collected by Faraday efficiency measurements and drainage was quantified using a measuring cylinder. A current density of 500 mA cm^{-2} was applied during oxygen collection.

The Mott-Schottky curves were tested in the abovementioned three-electrode instrument and acquired over an AC frequency of 1 kHz and 2 kHz with the potential region of 0.4–1.2 V (vs. Ag/AgCl). The Mott-Schottky technique is an electrochemical test method for evaluating the doping degree and flat-band potential of a material, and can also be used to observe thin films and single-crystal electrodes. The basic principle is to obtain a Mott-Schottky curve by measuring the capacitance value at different DC bias voltages. When a catalytic material is in contact with an electrolyte, a space charge region is formed on its surface, and the capacitance of this region is related to the doping concentration of the semiconductor, flat-band potential, and other parameters, which can be described by the Mott-Schottky equation:[1]

$$\frac{1}{C_{SC}^2} = \frac{2}{\varepsilon\varepsilon_0 A^2 e N_D}\left(E - E_{FB} - \frac{kT}{e}\right)$$

(1)

where ε is the dielectric constant of the material, ε_0 ($8.85E - 12\ F\ m^{-1}$) is the vacuum permittivity, A (m) is the exposed area of the material, e ($1.60E - 19\ C$) is the electronic charge, N_D is the doping density, E is the applied DC offset, E_{FB} is the flatband potential, k ($1.38E - 23\ J\ K^{-1}$) is the Boltzmann constant, and T (K) is the temperature. By drawing $\frac{1}{C^2}$ and V, the Mott-Schottky curve can be obtained, and the relevant parameters can then be extracted from information such as the slope and intercept of the curve.

To evaluate the electrochemical surface area (ECSA), cyclic voltammetry (CV) measurements were made. Scan rates of 20, 40, 60, 80, 100 mV s^{-1} were used, which helped to estimate the double layer capacitance (C_{dl}) of the sample. According to the relationship

$$ECSA = C_{dl}\ /\ Cs$$

(2)

C_s is defined as the specific capacitance of the sample, or the capacitance of an atomically smooth planar surface of the material per unit area under identical electrolyte conditions.[2] Specific capacitances have been measured for various metal electrodes in acidic and alkaline solutions. Typical values reported range from C_s = 0.015-0.110 mF/cm² in H_2SO_4, and C_s = 0.022–0.130 mF/cm² in NaOH and KOH solutions. For our estimates of surface area, we use general specific capacitances of 0.035mF/cm² in 1 M H_2SO_4 and 0.040 mF/cm² in 1 M NaOH, based on typical reported values.[3]
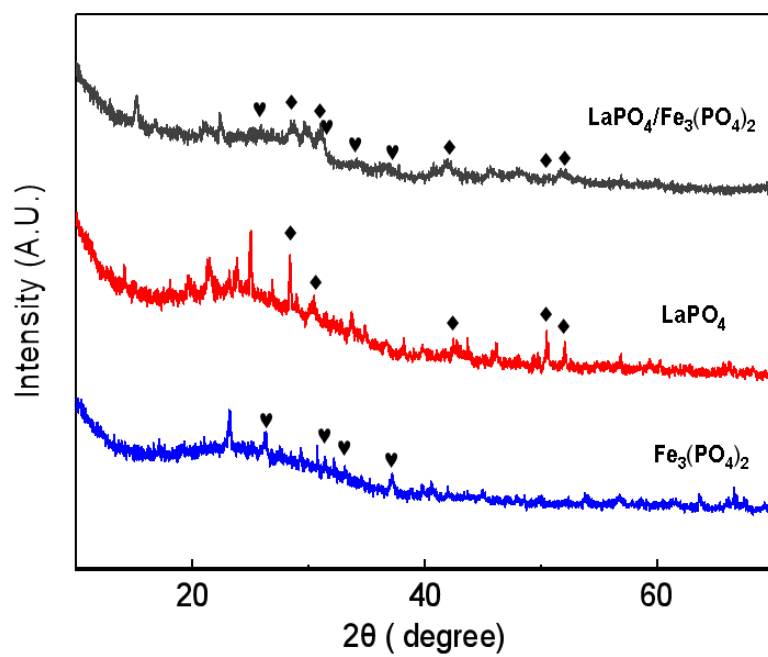
Figure S1. XRD patterns of the single phase of $LaPO_4$, $Fe_3(PO_4)_2$ versus the composite phase of $LaPO_4/Fe_3(PO_4)_2$.
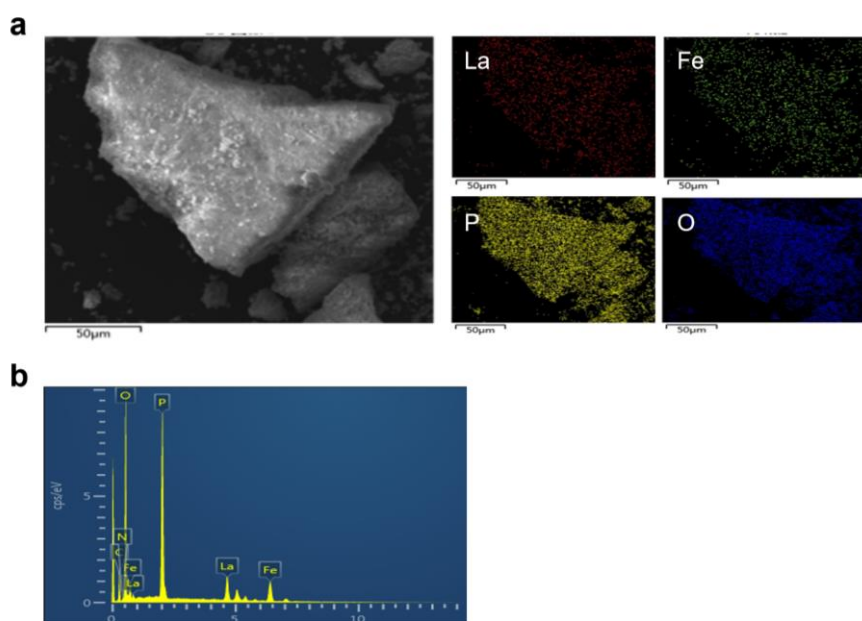
Figure S2. (a) Elemental mapping images of LaPO$_4$/Fe$_3$(PO$_4$)$_2$. (b) Energy dispersive spectroscopy (EDS) spectra of LaPO$_4$/Fe$_3$(PO$_4$)$_2$ catalyst.
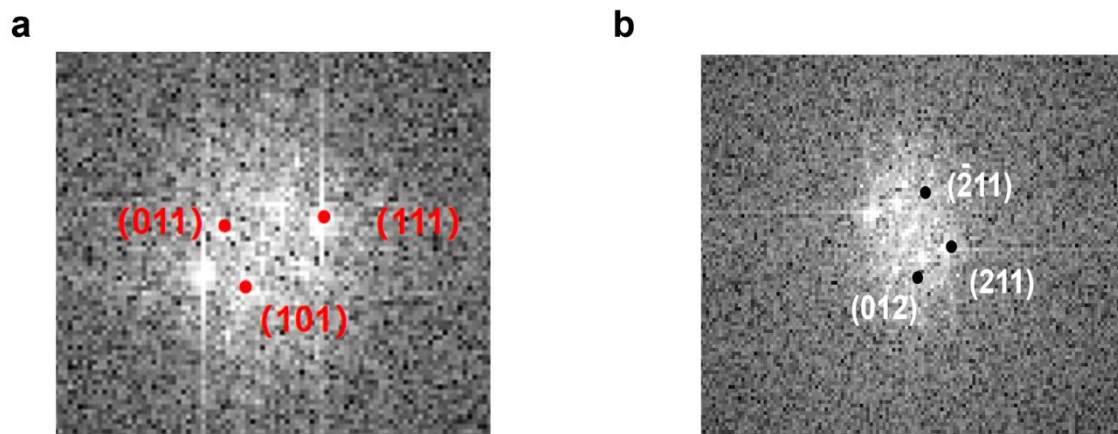
Figure S3. (a) the fast Fourier transform (FFT) image of the LaPO$_4$ nanocrystalline region.

(b) the fast Fourier transform (FFT) image of the Fe$_3$(PO$_4$)$_2$ nanocrystalline region.
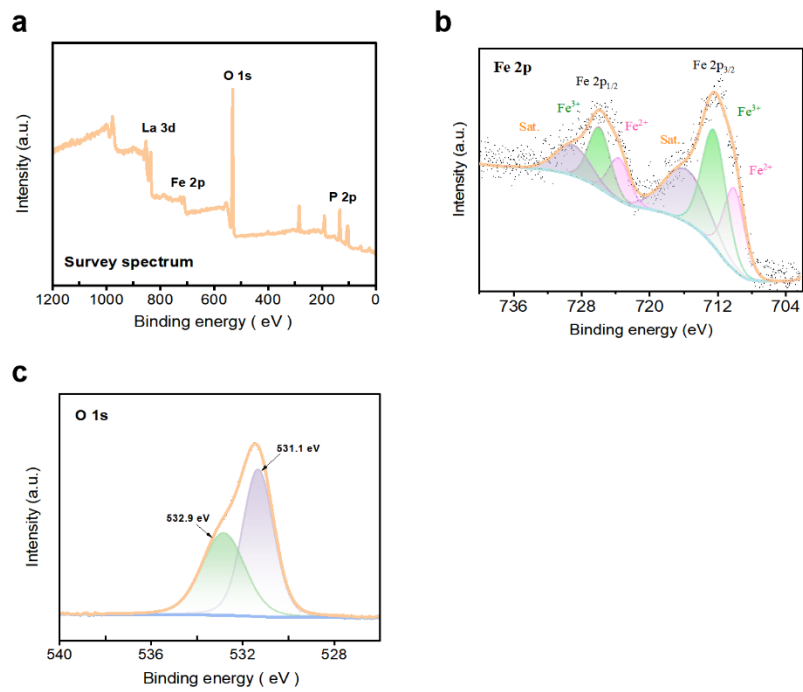
Figure S4. (a) Full XPS spectrum of $LaPO_4/Fe_3(PO_4)_2$; (b) XPS spectra of Fe 2p; (c) XPS spectra of O 1s.
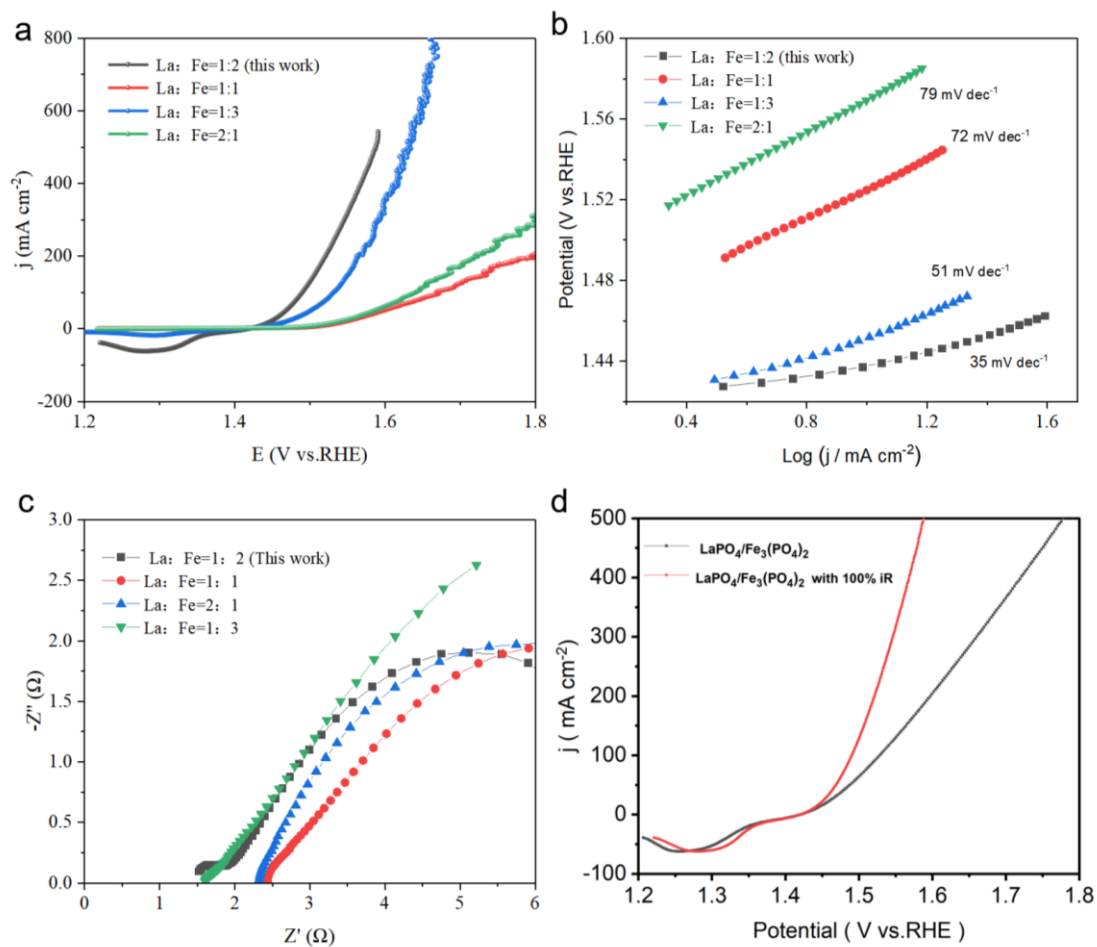
Figure S5. (a) OER polarization curves for LaPO$_4$/Fe$_3$(PO$_4$)$_2$ ratios of 1:2, 1:1, 1:3, and 2:1 with 100% iR compensation. (b). The corresponding Tafel slopes of the catalysts. (c). The Nyquist plots of the catalysts. (d). OER polarization curves of LaPO$_4$/Fe$_3$(PO$_4$)$_2$ with 100% (red line) and without (black line) iR compensation.
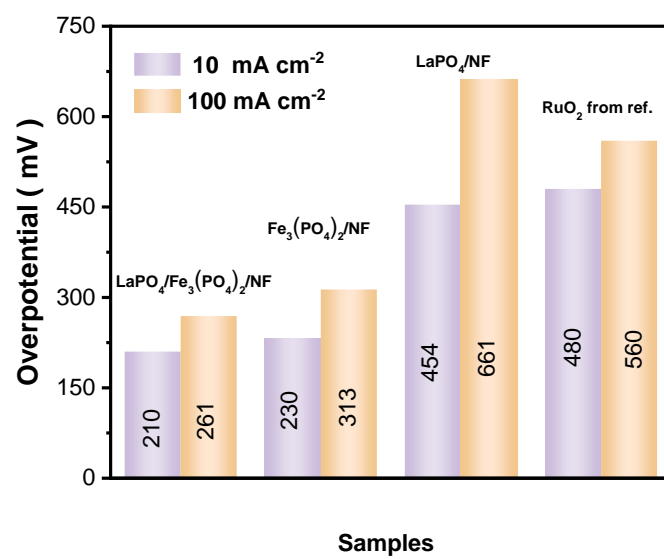
Figure S6. The overpotential of various catalysts at 10 and 100 mA cm^{-2}.

**a**

b

LaPO$_4$/Fe$_3$(PO$_4$)$_2$

RpY0 = 182 mMho*s^(1/2)
R = 472 mΩ

L = 0.00 H   Rs
R = 1.25 Ω

CPE
Y0 = 19.4 mMho*s^N
N = 0

C = 110 kF

c

Fe$_3$(PO$_4$)$_2$

Rp   Y0 = 125 mMho*s^(1/2)
R = 642 mΩ

L = 0.00 H   Rs
R = 1.21 Ω

CPE
Y0 = 621 μMho*s^N
N = 0

C = 1.80 F

d

LaPO$_4$

RpY0 = 25.8 mMho*s^(1/2)
R = 1.41 Ω

L = 0.00 H   Rs
R = 691 mΩ

CPE
Y0 = 21.1 mMho*s^N
N = 0

C = 110 kF
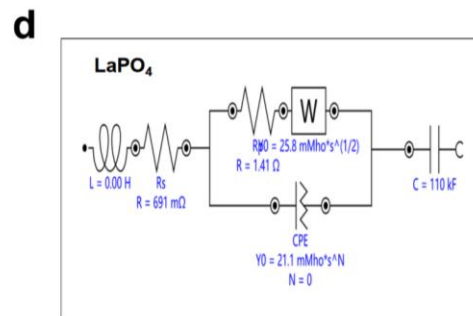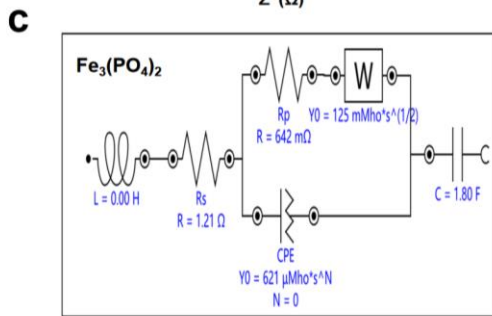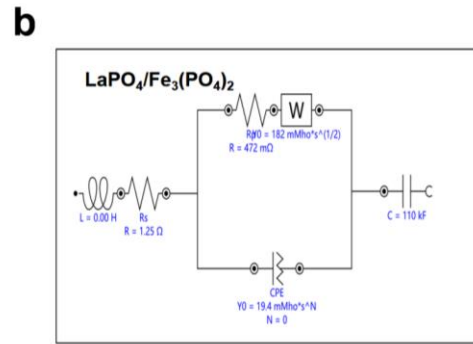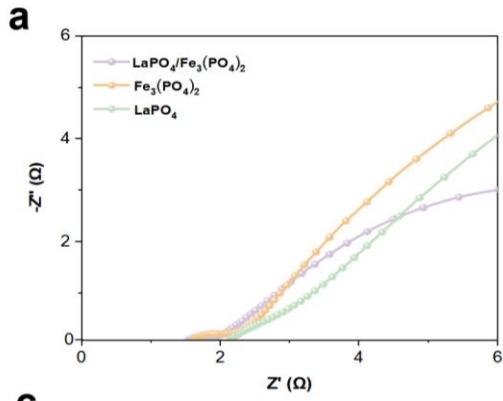
Figure S7. (a) The Nyquist plots of $LaPO_4/Fe_3(PO_4)_2$, $Fe_3(PO_4)_2$, $LaPO_4$. (b) Equivalent fit circuit diagram of $LaPO_4/Fe_3(PO_4)_2$. (c) $Fe_3(PO_4)_2$, (d) $LaPO_4$.

Figure S8. Water displacement method apparatus.
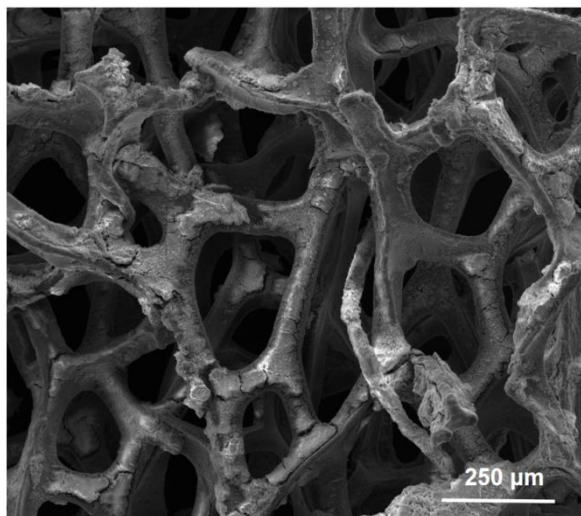
Figure S9. SEM image of a sample of LaPO$_4$/Fe$_3$(PO$_4$)$_2$ catalyst attached to nickel foam after long-term stability testing.
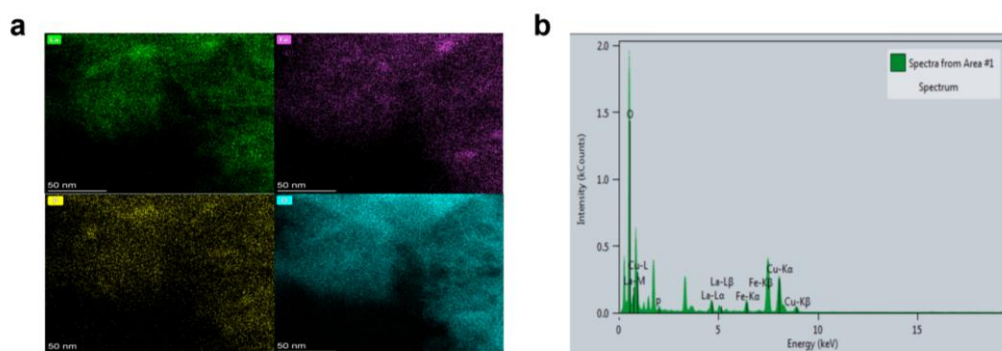
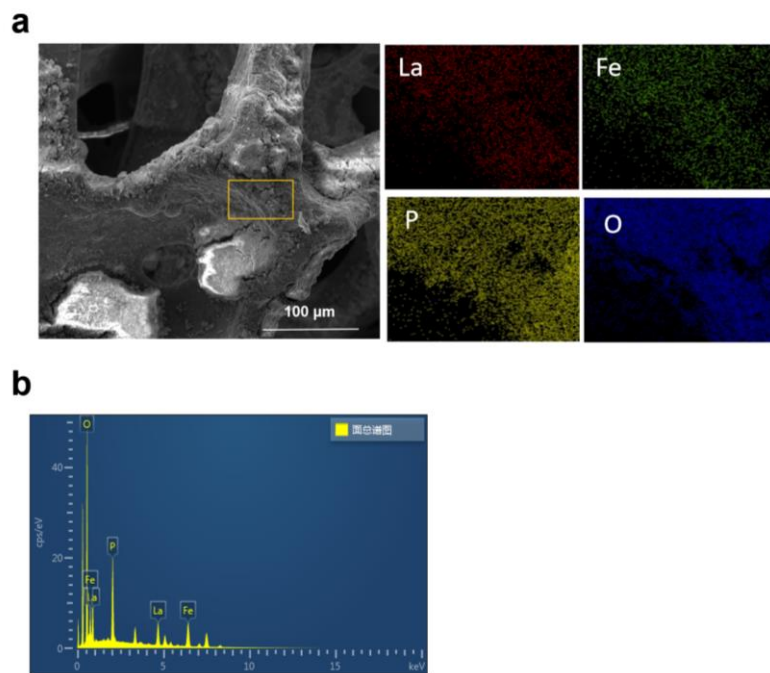**Figure S10.** (a) The high-angle annular dark-field STEM image of the corresponding element mapping images, and (b) Energy dispersive spectroscopy (EDS) spectra.
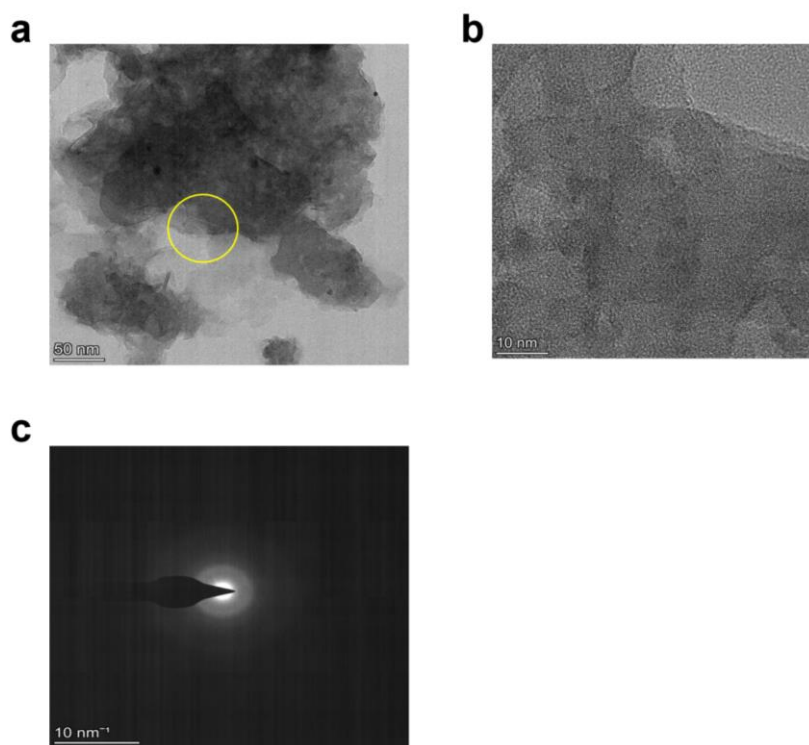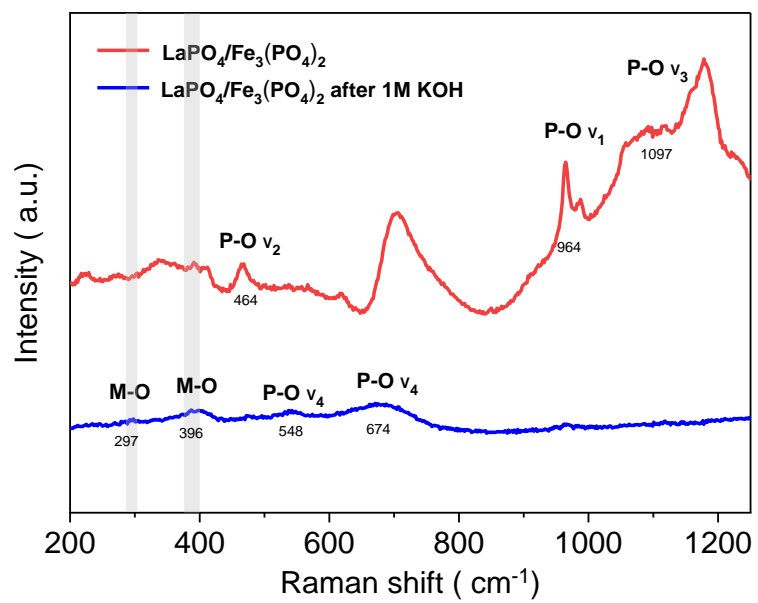
Figure S11. (a), (b) TEM images of $LaPO_4/Fe_3(PO_4)_2$ catalyst samples after long-term stability test. (c) SAED pattern of the amorphous substrate.

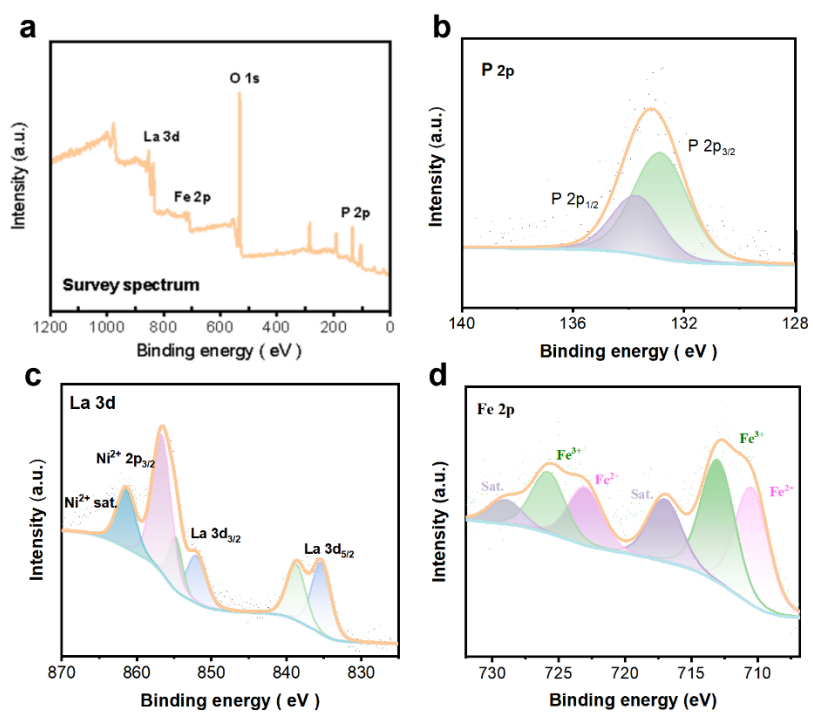**Figure S12.** (a) Elemental mapping images of LaPO$_4$/Fe$_3$(PO$_4$)$_2$ catalyst samples after long-term stability test. (b) Energy dispersive spectroscopy (EDS) spectra of after electrochemical test of LaPO$_4$/Fe$_3$(PO$_4$)$_2$ catalyst.
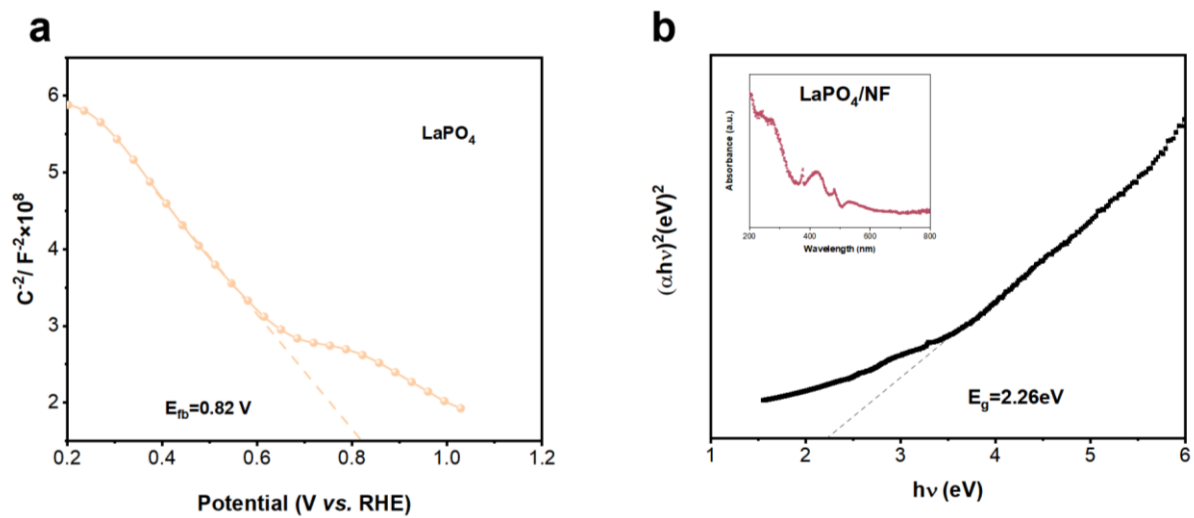
Figure S13. Raman characterization of $LaPO_4/Fe_3(PO_4)_2$ before and after OER reaction.
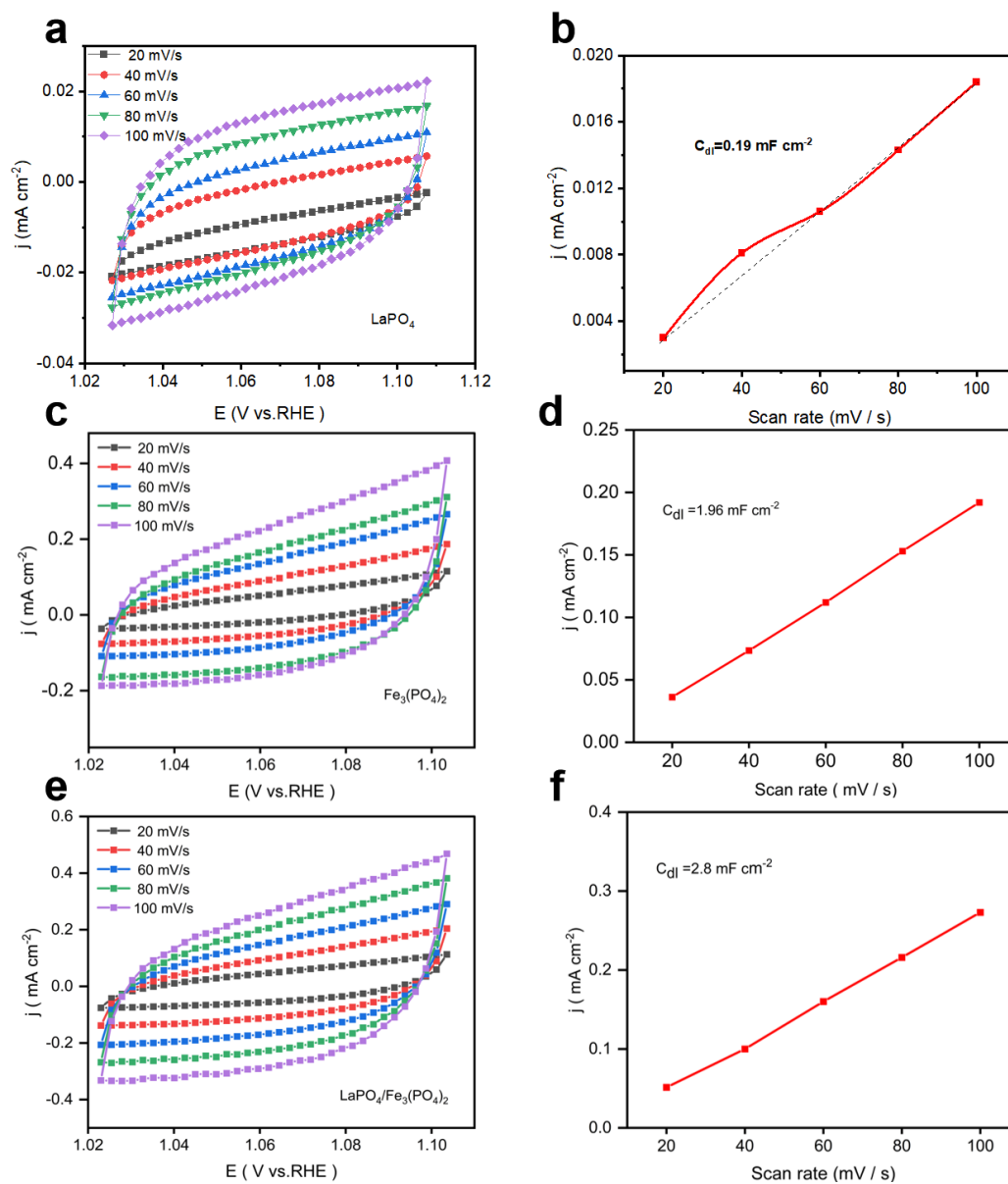
Figure S14. (a) Full XPS spectrum of LaPO$_4$/Fe$_3$(PO$_4$)$_2$ after long-term stability test. (b) XPS spectra of P 2p, (c) La 3d, (d) Fe 2p after long-term stability test.
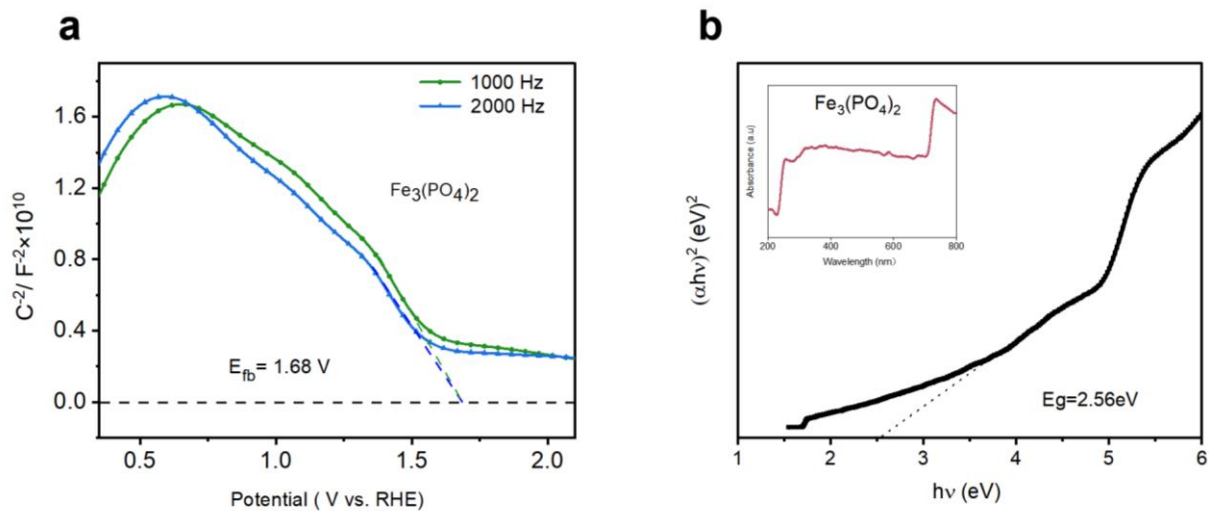
Figure S15. (a) Mott-Schottky curve of $Fe_3(PO_4)_2$ measured at 1000 Hz and 2000 Hz. (b) the Tauc plots of $Fe_3(PO_4)_2$.

Figure S16. (a) Mott-Schottky curve of LaPO$_4$ measured at 1000 Hz. (b) the Tauc plots of LaPO$_4$.

Figure S17. CV curves with the scan rates from 20 to 100 mV s^{-1} in 1.0 M KOH: (a) LaPO$_4$, (c) Fe$_3$(PO$_4$)$_2$, and (e) LaPO$_4$/Fe$_3$(PO$_4$)$_2$. Cdl values of (b) LaPO$_4$, (d) Fe$_3$(PO$_4$)$_2$, and (f) LaPO$_4$/Fe$_3$(PO$_4$)$_2$.

1   X. Lu, Z. Ma, Y. Chang, S. Wang, X. Li, D. Xu, J. Bao and Y. Liu, *Adv. Mater.*, 2024, **36**, 2313057.

2   K. Ji, J. Wang and P. Yang, *ACS Appl. Nano Mater.*, 2023, **6**, 7931-7941.

3   C. C. L. McCrory, S. Jung, J. C. Peters and T. F. Jaramillo, *J. Am. Chem. Soc.*, 2013, **135**, 16977-16987.